Supporting Information

Stabilization of Surface and Lattice Structure for $LiNi_{0.83}Co_{0.12}Mn_{0.05}O_2$ via B_2O_3 Atomic Layer Deposition and Post-Annealing

Jiawei Li, Junren Xiang, Ge Yi, Zhijia Hu, Xiao Liu*, Rong Chen*

State Key Laboratory of Intelligent Manufacturing Equipment and Technology, School of Mechanical Science and Engineering, Huazhong University of Science and Technology, Wuhan 430074, Hubei, People's Republic of China.

1. Calculation method of B_2O_3 coatings' average thickness

The average thicknesses of the B_2O_3 coatings can be calculated through the total volume of the B_2O_3 and the total surface area of the particles. The total volume of B_2O_3 coatings can be calculated via the mass and density of B_2O_3 coatings. The mass of the B_2O_3 coatings can be calculated via the concentration of the B and the mass of the particles. Hence, the calculation formula can be derived as below:

$$T = C(2U_B+3U_O)/2\rho AU_B$$

T – Average thicknesses of B_2O_3 coatings;

C – B mass concentration in particles;

A – Specific surface area of particles;

ρ – Density of B_2O_3, 1.84 g/cm^3;

U_B – atomic mass of B, 11;

U_O – atomic mass of O, 16.

Table S1. Parameters of SC83, LiOH, and Li_2CO_3 particles.

Particles	B Concentration (‰)	Specific Surface Area (m^2/g)
SC83	0.544	0.64
LiOH	8.677	2.68
Li_2CO_3	0.240	0.36

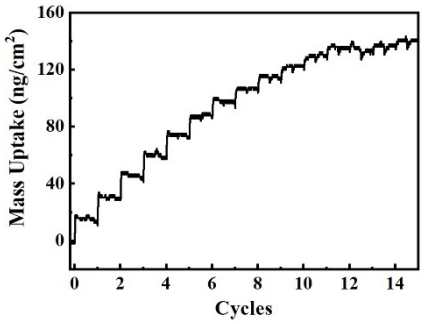

Figure S1. Mass uptake during the B_2O_3 ALD on the SC83 particles.

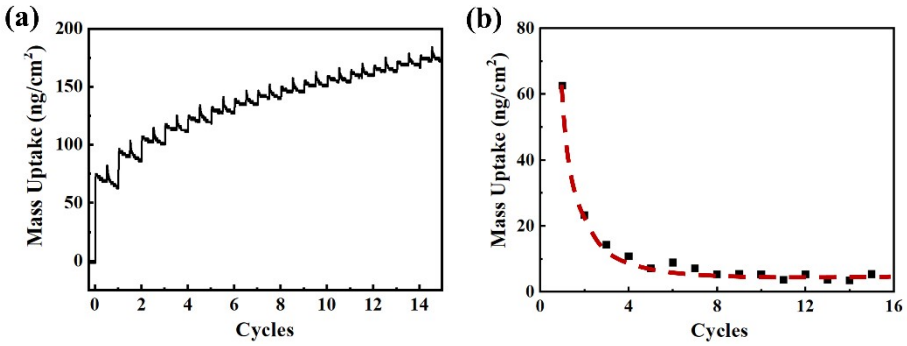

Figure S2. (a) Mass uptake during the B_2O_3 ALD on the Al_2O_3. (b) Mass uptake from each B_2O_3 ALD cycle on the Al_2O_3.

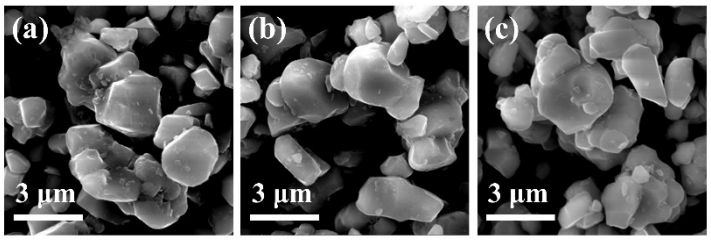

Figure S3. SEM images of the (a) bare, (b) 6B and (c) 6B-A SC83 particles.

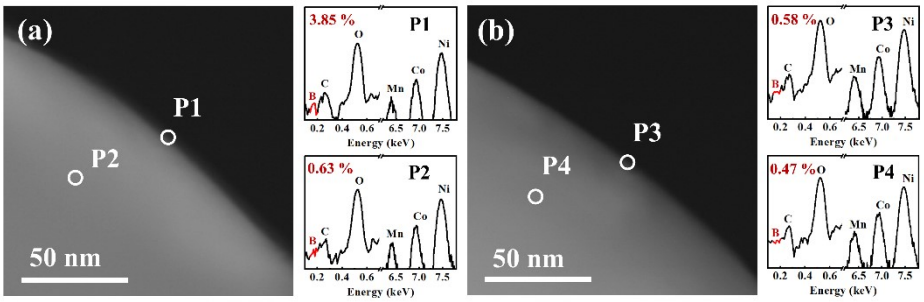

Figure S4. STEM images of the (a) 6B and (b) 6B-A SC83 particles. The EDS spectra of the marked locations are shown at the right of the corresponding STEM images.

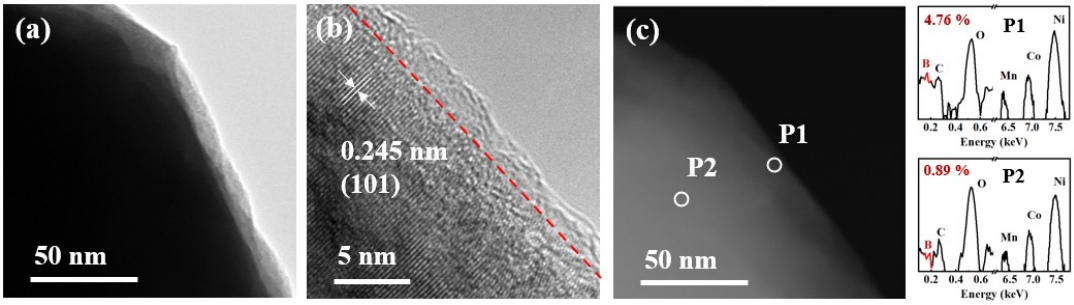

Figure S5. (a) TEM and (b) HR-TEM and (c) STEM images of the 12B SC83 particles. The EDS spectra of marked locations are shown at the right of the corresponding STEM images

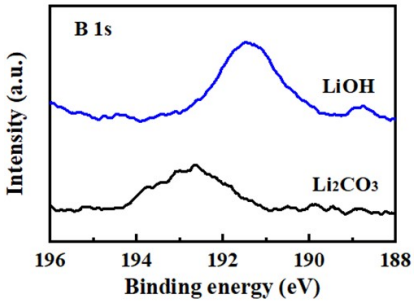

Figure S6. B 1s XPS spectra of the B_2O_3 coated Li_2CO_3 and LiOH with 6 ALD cycles.

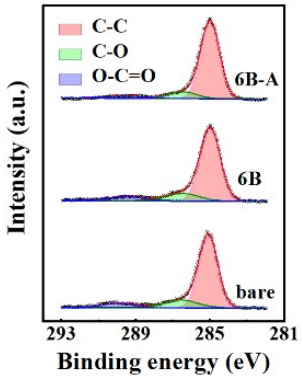

Figure S7. C 1s XPS spectra of the bare, 6B and 6B-A SC83 particles.

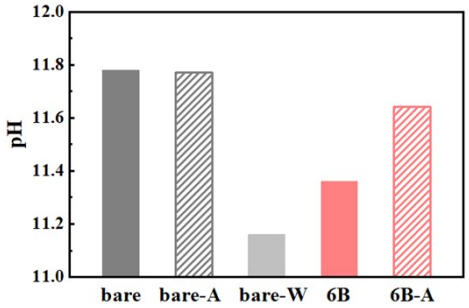

Figure S8. pH of the bare, bare-A, bare-W, 6B and 6B-A SC83 slurry.

The SC83 particles in the bare-W SC83 slurry come from the bare SC83 particles after being washed by deionized water, which have no attached alkaline compounds. The bare-W SC83 slurry still shows basicity. It is attributed to the H^+ in water exchange the Li^+ in the SC83, which induces the OH^- in the bare-W SC83 slurry[1]. The pH of the 6B SC83 slurry is higher than the bare SC83 slurry, while lower than the bare-W SC83 slurry. It indicates the alkaline compounds are reduced while still exist on the surface of the SC83. Besides, the pH of the 6B SC83 slurry is lower than the 6B-A SC83 slurry, which is attributed to the B_2O_3 coatings on the 6B SC83 dissolving and consuming the OH^- in the slurry. For 6B-A SC83, the B_2O_3 coatings have been transformed into B^{3+} doping. Hence, the pH of 6B SC83 slurry is lower than the 6B-A SC83 slurry.

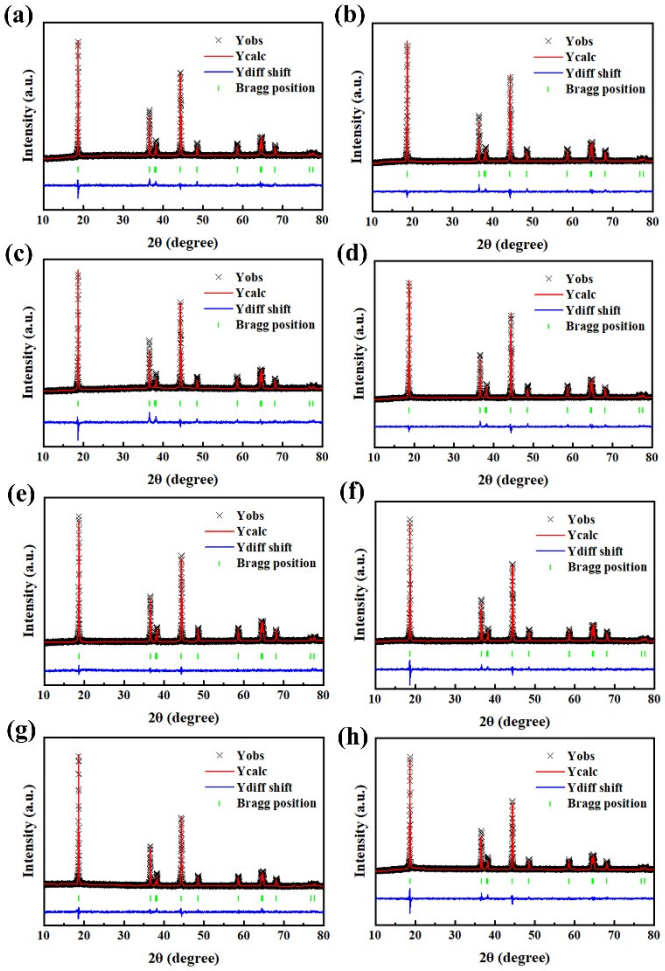

Figure S9. XRD Rietveld refinements of the (a) bare, (b) 2B, (c) 6B, (d) 12B, (e) bare-A, (f) 2B-A, (g) 6B-A, (h)12B-A SC83 particles.

Table S2. Lattice parameters of the bare, B_2O_3 ALD coated, annealed, and B_2O_3 ALD coated coupled with annealed SC83 particles.

Sample	*a* (Å)	*c* (Å)	V (Å^3)	Ni_{Li} (%)	R_{wp} (%)	R_p (%)
bare	2.8717	14.1820	101.29	4.60	3.75	2.65
2B	2.8716	14.1816	101.28	4.72	2.81	2.08
6B	2.8717	14.1820	101.28	4.67	4.26	2.85
12B	2.8717	14.1821	101.28	4.55	2.84	2.12
bare-A	2.8717	14.1820	101.29	4.46	2.97	2.19
2B-A	2.8724	14.1862	101.36	2.80	3.54	2.42
6B-A	2.8742	14.1964	101.56	1.43	3.26	2.48
12B-A	2.8740	14.1952	101.55	2.23	4.04	2.73

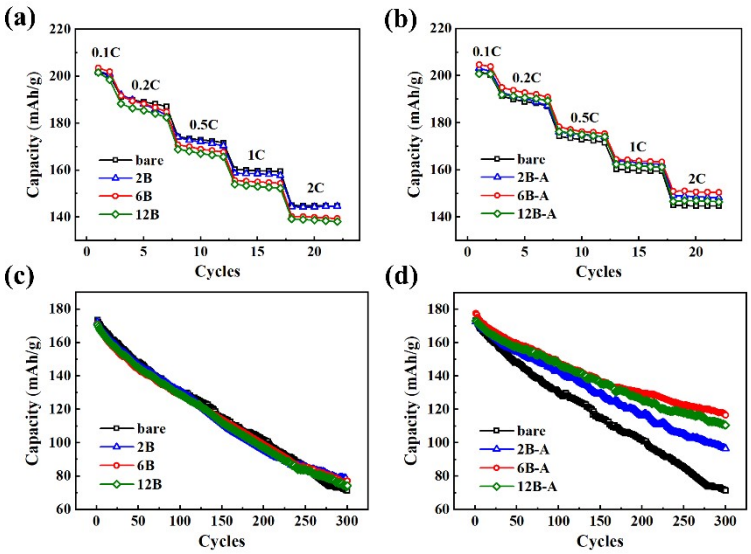

Figure S10. (a) Rate capability of the bare, 2B, 6B, and 12B SC83 cathodes. (b) Rate capability of the bare, 2B-A, 6B-A, and 12B-A SC83 cathodes. (c) Cycling stability of the bare, 2B, 6B, and 12B SC83 cathodes at 1C. (d) Cycling stability of the bare, 2B-A, 6B-A, and 12B-A SC83 cathodes at 1C.

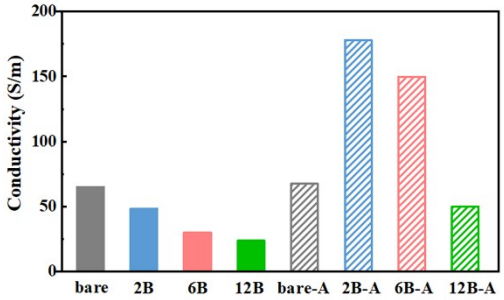

Figure S11. Electronic conductivity of the bare, annealed, annealed, B_2O_3 ALD coated coupled with annealed SC83 particles at 20 MPa.

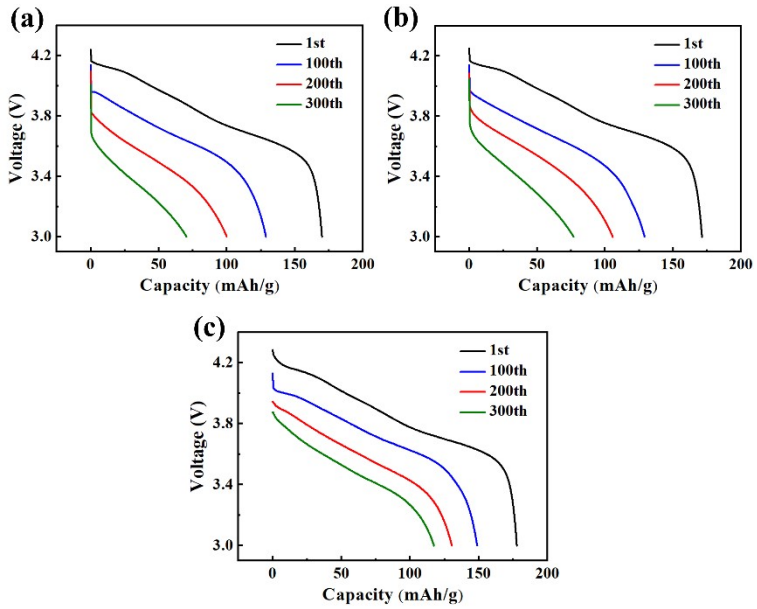

Figure S12. Discharge curves of the (a) bare, (b) 6B, and (c) 6B-A SC83 cathodes during the cycling.

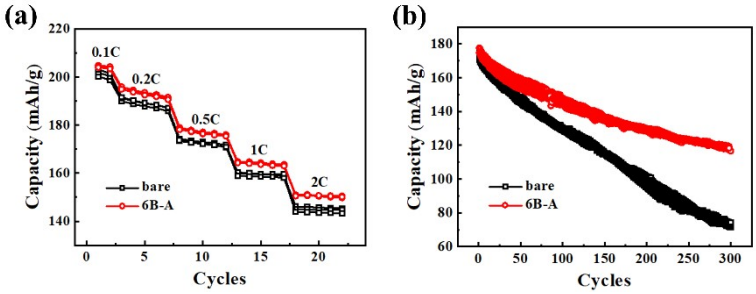

Figure S13. Repeated (a) rate capability and (b) cycling stability of bare and 6B-A SC83 cathodes. Each cathode repeats in three cells.

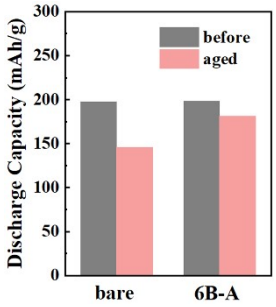

Figure S14. Discharge capacity of the bare and 6B-A SC83 cathodes before and after storage at 60°C for 12h.

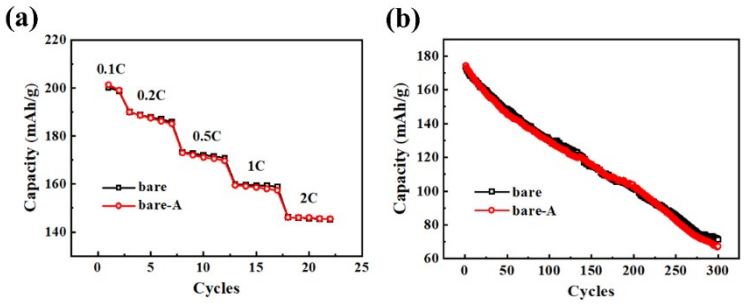

Figure S15. (a) Rate capability of the bare and bare-A SC83 cathodes. (b) Cycling stability of the bare and bare-A SC83 cathodes at 1C.

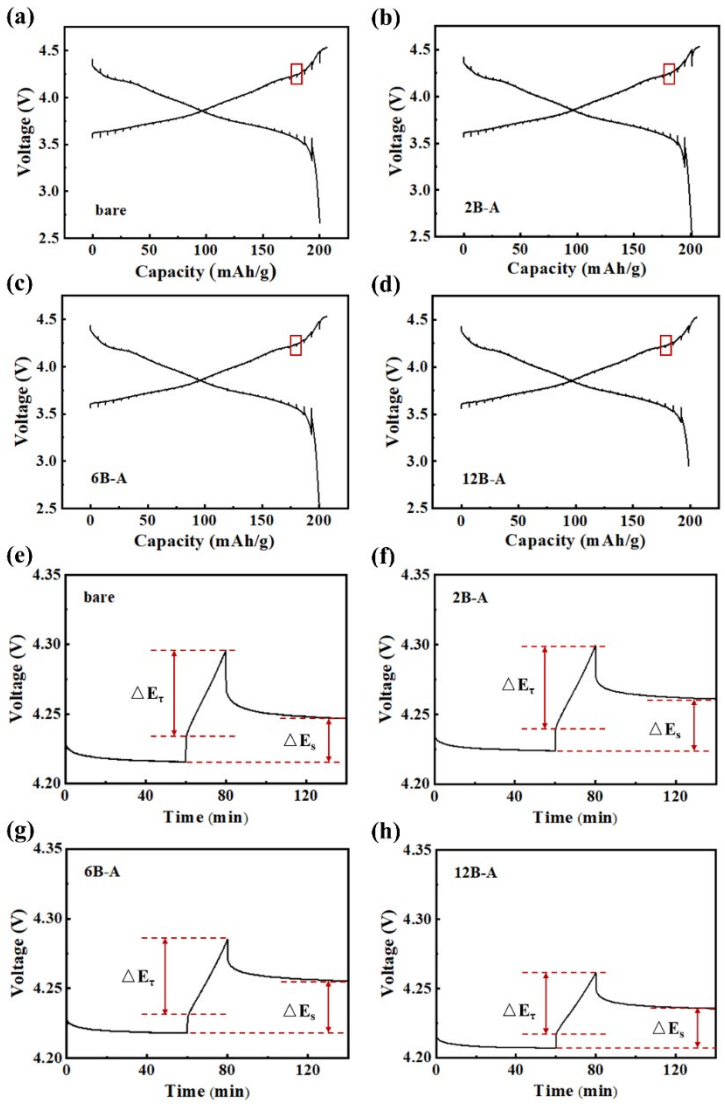

Figure S16. GITT curves of the (a) bare, (b) 2B-A, (c) 6B-A and (d) 12B-A SC83 cathodes. Enlarged voltage profiles for a single step of GITT curves during the charge process of the(e) bare, (f) 2B-A, (g) 6B-A and (h) 12B-A SC83 cathodes.

The Li^+ diffusivity (D_{Li^+}) is calculated by the recorded GITT curves. The coin cells were firstly given a galvanostatic current of 0.1C in 20 minutes, and then followed by a relaxation time of 60 minutes to reach electrochemical equilibrium. This operation is repeated until the end of the voltage window. Figure S16e shows a single step of GITT curves during the charge process of the bare SC83 cathode. D_{Li^+} can be calculated using the simplified formula as follow:

$$D_{Li^+} = 4\pi^{-1}(m_B V_M / M_B A)^2 (\triangle E_s / \triangle E_\tau)^2$$

m_B – mass loading of SC83, g;

V_M – molar volume of SC83, cm^3/mol;

M_B – molecular weight of SC83, g/mol;

A – contact area of the electrode, cm^2;

$\triangle E_s$ – voltage difference between the end of adjacent relaxation step;

$\triangle E_\tau$ – voltage difference between the start and end of each charge or discharge step;

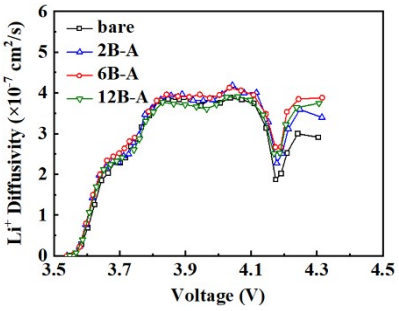

Figure S17. Li^+ diffusivity of the bare, 2B-A, 6B-A, and 12B-A SC83 cathodes during the discharge process.

The result is similar with the Li^+ diffusivity of the bare, 2B-A, 6B-A, and 12B-A SC83 cathodes during the charge process. The difference is that the Li^+ diffusivity of all SC83 cathodes during the discharge process is higher than which during the charge process. It is attributed to higher kinetics for Li^+ insertion than extraction in the highly delithiated SC83 cathode. Besides, an obvious valley is found around 4.2V, which is attributed to lower kinetics for Li^+ insertion during the phase transition process compared to the solid solution process.

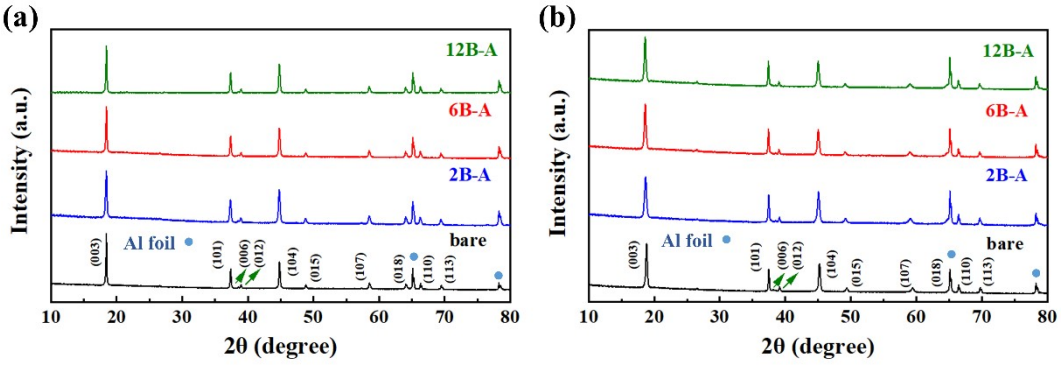

Figure S18. XRD patterns of the bare, 2B-A, 6B-A and 12B-A SC83 cathodes at (a) 4.1 V and (b) 4.4 V.

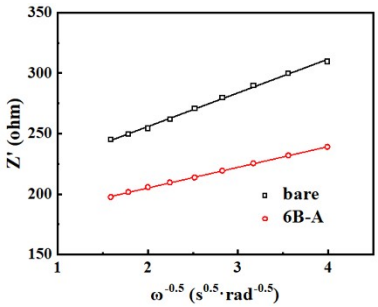

Figure S19. Z' vs $\omega^{-0.5}$ plots in the low-frequency region obtained from the EIS spectra of the bare and 6B-A SC83 cathodes in Figure 6c.

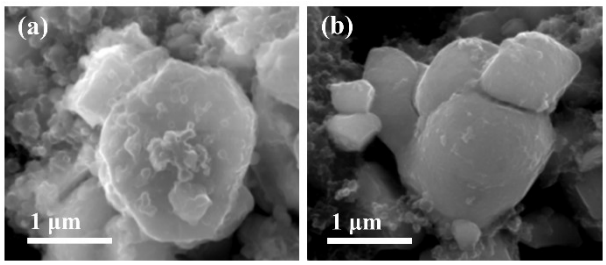

Figure S20. SEM images of the (a) bare and (b) 6B-A SC83 cathodes recovered from the coin cells after cycling.

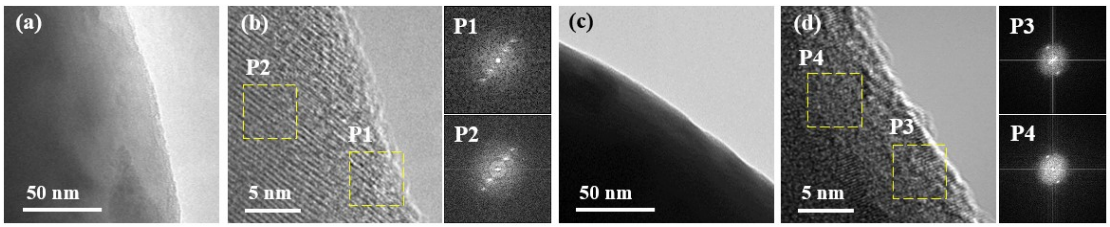

Figure S21. (a) TEM and (b) HR-TEM of the bare SC83 cathode recovered from the coin cells before cycling. (c) TEM and (d) HR-TEM images of the 6B-A SC83 cathode recovered from the coin cells before cycling. HR-TEM images of the 6B-A SC83 cathode recovered from the coin cells after cycling. The FFT spectra of the marked locations are shown at the right of the corresponding HR-TEM images.

Table S3. The capacity release ability of Ni-rich cathodes at 0.1 and 1 C in this study compared to literature reports.

Year	Cathode material	Modification strategy	Test Conditions	0.1C Capacity	1C Capacity
This work	**single-crystal $LiNi_{0.83}Co_{0.12}Mn_{0.05}O_2$**	**B_2O_3 ALD and post-annealing**	**3.0-4.5 V, 21 ℃**	**204.7 mAh/g**	**177.6 mAh/g**
2022[2]	Polycrystalline $LiNi_{0.8}Co_{0.1}Mn_{0.1}O_2$	H_3BO_3 wet coating and post-annealing	2.75-4.3 V, 25 ℃	200.5 mAh/g	170 mAh/g
2021[3]	Polycrystalline $LiNi_{0.8}Co_{0.1}Mn_{0.1}O_2$	H_3BO_3 wet coating and post-annealing	3.0-4.3 V, 25 ℃	196.9 mAh/g	172.5 mAh/g
2020[4]	polycrystalline $LiNi_{0.83}Co_{0.12}Mn_{0.05}O_2$	B_2O_3 dry coating and post-annealing	2.5-4.3 V, 25 ℃	204 mAh/g	175 mAh/g
2022[5]	polycrystalline $LiNi_{0.8}Co_{0.1}Mn_{0.1}O_2$	B^{3+} doping	3.0-4.3 V, 25 ℃	180 mAh/g	138.5 mAh/g
2023[6]	polycrystalline $LiNi_{0.85}Mn_{0.09}Al_{0.06}O_2$	$LilnO_2$ coating, In and Sn doping	2.7-4.5 V, 30 ℃	N/A	183 mAh/g
2022[7]	single-crystal $LiNi_{0.83}Co_{0.12}Mn_{0.05}O_2$	Li_2TiO_3 coating and Ti doping	2.7-4.3 V, 25 ℃	205.9 mAh/g	176 mAh/g
2022[8]	single-crystal $LiNi_{0.8}Co_{0.1}Mn_{0.1}O_2$	$BaTiO_3$ coating	2.75-4.3 V, 25 ℃	190.5 mAh/g	163.6 mAh/g
2020[9]	polycrystalline $LiNi_{0.91}Co_{0.06}Mn_{0.03}O_2$	SO_2 treatment	2.7-4.3 V, 25 ℃	216.1 mAh/g	180.8 mAh/g
2022[10]	polycrystalline $LiNi_{0.8}Co_{0.15}Al_{0.05}O_2$	F^- doping	2.8-4.3 V 25 ℃	197.5 mAh/g	171 mAh/g
2021[11]	polycrystalline $LiNi_{0.815}Co_{0.15}Al_{0.035}O_2$	Zn^{2+} doping	2.7-4.3 V 25 ℃	191.8 mAh/g	167 mAh/g

2019[12]	polycrystalline $LiNi_{0.8}Co_{0.1}Mn_{0.1}O_2$	Na^+ doping	2.8-4.3 V 25 ℃	191.6 mAh/g	173.6 mAh/g

References

1. D. Pritzl, T. Teufl, A. T. S. Freiberg, B. Strehle, J. Sicklinger, H. Sommer, P. Hartmann and H. A. Gasteiger, *J. Electrochem. Soc.*, 2019, **166**, A4056-A4066.
2. Y. Su, L. Li, L. Chen, L. Wang, Y. Lu, Q. Zhang, L. Bao and F. Wu, *ACS Appl. Energy Mater.*, 2022, **5**, 2231-2241.
3. L. You, B. Chu, G. Li, T. Huang and A. Yu, *J. Power Sources*, 2021, **482**, 228940.
4. Q. Li, W. Zhuang, Z. Li, S. Wu, N. Li, M. Gao, W. Li, J. Wang and S. Lu, *ChemElectroChem*, 2020, **7**, 998-1006.
5. C. Roitzheim, L.-Y. Kuo, Y. J. Sohn, M. Finsterbusch, S. Möller, D. Sebold, H. Valencia, M. Meledina, J. Mayer, U. Breuer, P. Kaghazchi, O. Guillon and D. Fattakhova-Rohlfing, *ACS Appl. Energy Mater.*, 2021, **5**, 524-538.
6. Y. Lv, S. Huang, S. Lu, T. Jia, Y. Liu, W. Ding, X. Yu, F. Kang, J. Zhang and Y. Cao, *Chem. Eng. J.*, 2023, **455**, 140652.
7. Z. Yang, L. Chen, H. Zhu, Y. Zhu, H. Jiang and C. Li, *J. Mater. Sci. Technol.*, 2022, **125**, 192-197.
8. F. Jin, X. Xue, Y. Zhao, L. Shi, Z. Wang, M. Zhang, Y. Wang, J. Zhu and S. Yuan, *J. Colloid Interface Sci.*, 2022, **619**, 65-74.
9. W. M. Seong, K. H. Cho, J. W. Park, H. Park, D. Eum, M. H. Lee, I. S. Kim, J. Lim and K. Kang, *Angew. Chem. Int. Ed.*, 2020, **59**, 18662-18669.
10. J. Wang, C. Liu, G. Xu, C. Miao, M. Wen, M. Xu, C. Wang and W. Xiao, *Chem. Eng. J.*, 2022, **438**, 135537.
11. C. Xu, W. Xiang, Z. Wu, L. Qiu, Y. Ming, W. Yang, L. Yue, J. Zhang, B. Zhong, X. Guo, G. Wang and Y. Liu, *Chem. Eng. J.*, 2021, **403**, 126314.
12. T. He, L. Chen, Y. Su, Y. Lu, L. Bao, G. Chen, Q. Zhang, S. Chen and F. Wu, *J. Power Sources*, 2019, **441**, 227195.